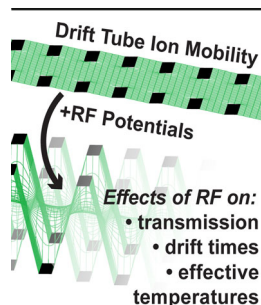


## RESEARCH ARTICLE

# Radio-Frequency (rf) Confinement in Ion Mobility Spectrometry: Apparent Mobilities and Effective Temperatures

Samuel J. Allen, Matthew F. Bush

Department of Chemistry, University of Washington, Box 351700, Seattle, WA 98195-1700, USA



**Abstract.** Ion mobility is a powerful tool for separating and characterizing the structures of ions. Here, a radio-frequency (rf) confining drift cell is used to evaluate the drift times of ions over a broad range of drift field strengths ( $E/P$ ,  $\text{V cm}^{-1} \text{Torr}^{-1}$ ). The presence of rf potentials radially confines ions and results in excellent ion transmission at low  $E/P$  (less than  $1 \text{ V cm}^{-1} \text{Torr}^{-1}$ ), thereby reducing the dependence of ion transmission on the applied drift voltage. Non-linear responses between drift time and reciprocal drift voltages are observed for extremely low  $E/P$  and high rf amplitudes. Under these conditions, pseudopotential wells generated by the rf potentials dampen the mobility of ions. The effective potential approximation is used to characterize this mobility dampening behavior, which can be mitigated by adjusting rf amplitudes and

electrode dimensions. Using SIMION trajectories and statistical arguments, the effective temperatures of ions in an rf-confining drift cell are evaluated. Results for the doubly charged peptide GRGDS suggest that applied rf potentials can result in a subtle increase (2 K) in effective temperature compared to an electrostatic drift tube. Additionally, simulations of native-like ions of the protein complex avidin suggest that rf potentials have a negligible effect on the effective temperature of these ions. In general, the results of this study suggest that applied rf potentials enable the measurement of drift times at extremely low  $E/P$  and that these potentials have negligible effects on ion effective temperature.

**Keywords:** Ion mobility spectrometry, Ion mobility mass spectrometry, Effective temperature, Native mass spectrometry

Received: 28 April 2016/Revised: 8 August 2016/Accepted: 11 August 2016/Published Online: 31 August 2016

## Introduction

Ion mobility (IM) is a gas-phase technique that separates ions based on their size, shape, and charge [1]. When used with mass spectrometry (MS), IM-MS enables the simultaneous characterization of structure and composition [2–5]. IM-MS has been used to characterize a broad range of analytes, including chemical warfare agents [6], organic compounds [7], drugs [8], peptides [9, 10], carbohydrates [11], lipids [12], proteins [13], and protein complexes [9, 14]. Although some recent mobility techniques such as traveling-wave [15] or trapped [16] IM can enable high

resolving power separations, electrostatic drift tube IM offers the advantage of direct determination of the mobility of the ion ( $K$ ) [17–19].

Implementations of electrostatic drift tubes typically include a series of stacked rings that are connected to a voltage divider network [18–22]. Direct-current (DC) potentials applied to the voltage divider network establish a constant DC gradient that ions experience as they traverse the drift region. The drift velocity of ions ( $v_D$ ) depends on the applied electric field ( $E$ ) and  $K$ :

$$v_D = KE = K \frac{V}{L} \quad (1)$$

where  $E$  is equal to the applied drift voltage ( $V$ ) divided by the length of the drift region ( $L$ ).  $K$  depends on the charge and shape of the ion.  $K$  values can be determined from the slopes of drift time ( $t_D$ ) versus reciprocal  $V$  plots:

**Electronic supplementary material** The online version of this article (doi:10.1007/s13361-016-1479-9) contains supplementary material, which is available to authorized users.

Correspondence to: Matthew F. Bush; e-mail: mattbush@uw.edu

$$t_D = \frac{L^2}{K} \frac{1}{V} \quad (2)$$

These experiments can be used to extract structural information by converting the measured  $K$  into a collision cross section ( $\Omega$ ) using the Mason-Schamp equation [23].

As ions traverse an electrostatic drift tube, a steady-state drift velocity is achieved from the force-balance of ion-neutral collisions and the applied electric field (Equation 1). During this time, ions also diffuse axially, which limits resolving power [24], and radially, which can decrease ion transmission [25]. One strategy to correct for radial diffusion is to position electrostatic lenses [17, 20, 26, 27] or an ion funnel [18, 19, 21, 22] after the drift tube to refocus ions. Ion funnels contain a constant DC gradient in addition to alternating rf (electrodynamic) potentials, similar to a stacked-ring ion guide [28], applied to incrementally decreasing inner diameter (i.d.) electrodes that refocus radially diffuse ions [29, 30]. Other implementations of rf confinement in IM devices include segmented-quadrupoles [31, 32], modified triple quadrupole instruments [33, 34], a stacked-ring ion guide with an applied staircase-like DC gradient [35], traveling-wave IM cells [15], trapped IM cells [16], a gridless-overtone mobility cell [36], structures for lossless ion manipulations (SLIM) [37], and rf-confining drift cells [9, 38]. rf-Confining drift cells contain a constant DC gradient, similar to an electrostatic drift tube, and alternating rf potentials applied to all electrodes, similar to a stacked-ring ion guide. rf-Confining drift cells enable direct and absolute determination of  $\Omega$  values [9, 38]. Studies have shown that  $\Omega$  values determined using rf-confining drift cells are similar to those determined using electrostatic drift tubes [9, 19, 38, 39].

Although the use of rf confinement with drift cells increases ion transmission, nonlinear responses between  $t_D$  and reciprocal  $V$  (Equation 2) have been observed. For example, the first implementation of an rf-confining drift cell [9] and a drift tube containing an ion funnel at the end of the drift region [18] both exhibited longer  $t_D$  than expected at lower  $V$ . Somewhat analogous results have been observed for periodically-focused drift tubes [40], which applied a uniform  $E$  across a series of ring electrodes that have smaller i.d. and larger thicknesses than those used for traditional electrostatic drift tubes [41–43]. These electrode geometries generate atypical ion drift motion and, consequently, more ion-neutral collisions that result in longer  $t_D$  than would be expected for traditional electrostatic drift tubes.

In native IMMS experiments, analysis of ions that have folded, native-like structures is used to evaluate structures and assemblies that reflect those in solution [5]. Activation of ions can lead to gas-phase unfolding that generates structures that have less memory of those in solution [17, 44, 45]. Assuming elastic ion-neutral collisions, the effective translational temperature ( $T_{eff}$ ) of ions in an electrostatic drift tube can be calculated from the drift-gas temperature ( $T_{gas}$ ) and  $v_D$ , which depends on the applied  $E$  [46]:

$$T_{eff} = T_{gas} + \frac{M}{3k_B} v_D^2 \quad (3)$$

where  $M$  is the mass of the neutral gas and  $k_B$  is the Boltzmann constant. For example,  $T_{eff}$  for potassium ions estimated from measurements as a function of  $E$  and Equation 3 agree well with  $T_{eff}$  estimated from ion-beam scattering measurements [47]. For electrostatic drift tube measurements performed well below the low-field limit [48], contributions from  $v_D$  to  $T_{eff}$  will be small.

Ions in electrodynamic IM experiments may experience high instantaneous fields; therefore, it is important to consider the effects of dynamic fields on the temperatures of those ions. For example, several studies have considered  $T_{eff}$  of ions in traveling-wave IM devices [49–51], which use a time-dependent DC “wave” and alternating rf potentials applied to all electrodes [15]. Estimates of  $T_{eff}$  using Equation 3 and applied  $E$  values in traveling-wave IM experiments can range from ~500 to 7300 K [49]. Using chemical thermometer ions,  $T_{eff}$  of these ions in traveling-wave IM devices were estimated to be up to 555 K [50] or 449 K [51]. In those examples, it is difficult to decouple the contributions of traveling-wave DC and rf potentials to the  $T_{eff}$  of ions.

Here, experimental measurements and ion simulations of an rf-confining drift cell are used to evaluate the effects of rf confinement on the transport properties of gas-phase ions. The advantages of rf-confining drift cells include control over the applied rf amplitude and DC gradient, which enable an evaluation of ion transport properties over a broad range of DC and rf potential environments. Generally, we find that increased rf amplitudes in a 5 mm i.d. rf-confining drift cell result in longer  $t_D$  at low drift field strengths ( $E/P$ ,  $V \text{ cm}^{-1} \text{ Torr}^{-1}$ , where  $P$  is pressure), whereas  $t_D$  in a 7 mm i.d. rf-confining drift cell depend weakly on rf amplitude. These mobility dampening effects in a 5 mm i.d. drift cell are a result of pseudopotential wells along the axis of transmission that have a more significant effect at lower  $E/P$ .  $T_{eff}$  of ions are estimated based on ion trajectory simulations and a new statistical approach that uses the distribution of relative ion-neutral speeds. Results for the doubly charged peptide GRGDS<sup>2+</sup> suggest that the presence of rf potentials has negligible effects on the  $T_{eff}$  of ions in a 7 mm i.d. rf-confining drift cell relative to that device with no rf potentials applied. In contrast,  $T_{eff}$  increases slightly (2 K) for those ions in a 5 mm i.d. rf-confining drift cell containing applied rf potentials.  $T_{eff}$  values are also estimated for  $E/P$  greater than the low-field limit, which show that higher  $E/P$  have a far more significant effect on  $T_{eff}$  than applied rf potentials. For comparison,  $T_{eff}$  were also estimated for the 17+ charge state of the native-like, homotetramer of avidin. In contrast to GRGDS<sup>2+</sup> results, rf-confining drift cell i.d. and applied rf potentials have no significant effect on the  $T_{eff}$  of these ions.

## Methods

GRGDS (490 Da, Waters Corporation 700005089) was diluted to 0.01 mg mL<sup>-1</sup> in 49.5/49.5/1 water/methanol/acetic acid solutions. The sample solution was

electrosprayed in positive ion mode through borosilicate capillaries (0.78 mm i.d.) that have one end pulled to a tip of 1 to 3  $\mu\text{m}$ . All measurements were performed using a modified Waters Synapt G2 HDMS in which the traveling-wave IM cell was replaced with an rf-confining drift cell as described previously [38]. Briefly, the rf-confining drift cell is 25.2 cm in length and consists of 168 gold-coated electrodes that are 0.5 mm thick and have center-to-center spacing of 1.5 mm. Two rf-confining drift cells were used that differ only in the i.d. of the electrodes (5 or 7 mm). Each electrode is connected to printed circuit boards containing voltage divider networks that establish a constant DC voltage gradient across the length of the drift cell. Additionally, rf potentials are applied to every electrode; the waveform applied to each electrode is  $180^\circ$  out of phase with that applied to the adjacent electrodes. The rf frequency was 2.8 MHz and the peak-to-peak rf amplitude ( $V_{PP}$ ) ranged from 15 to 200 V. All drift times were measured in 3.5 Torr helium gas.

Ion trajectories were simulated using SIMION 8.1 and the HS1 hard-sphere approximation for elastic ion-neutral collisions [52]. Briefly, the neutral gas has a Maxwell-Boltzmann distribution of velocities, which is a function of temperature. The probability of ion-neutral collision is a function of the mean free path, which is predicted using kinetic theory of gases as a function of pressure, temperature, and  $\Omega$ . Mean free paths of GRGDS $^{2+}$  and avidin $^{17+}$  ions were estimated using published  $\Omega$  values [38]. Unless specified, ion trajectories were modelled in 3.5 Torr helium gas. To reduce the cost of calculating the potential array during each step of the simulations, computational models used one-third the length (8.4 cm) and the same range of  $E/P$  ( $\text{V cm}^{-1} \text{Torr}^{-1}$ ) used experimentally.

## Results and Discussion

Here we use experiments and simulations to investigate the effects of rf confinement in an rf-confining drift cell. Experimental design and implementation of this rf-confining drift cell have been described previously [38]. The rf-confining potentials enable mobility measurements with transmission efficiencies that depend less on applied drift voltage compared with electrostatic drift tubes. For example, Fig. 1a shows an electrostatic drift tube, with analogous dimensions to the rf-confining drift cell discussed here. Ion trajectory simulations of the peptide GRGDS $^{2+}$  under a low  $E/P$  of  $0.507 \text{ V cm}^{-1} \text{Torr}^{-1}$  show that ions are readily lost prior to the end of the drift region due to diffusion in the radial directions. Ion trajectory simulations of GRGDS $^{2+}$  in an rf-confining drift cell under the same  $E/P$  show that the rf potentials in the drift region radially confine ions and increase ion transmission (Fig. 1b). The following sections evaluate the accuracy of

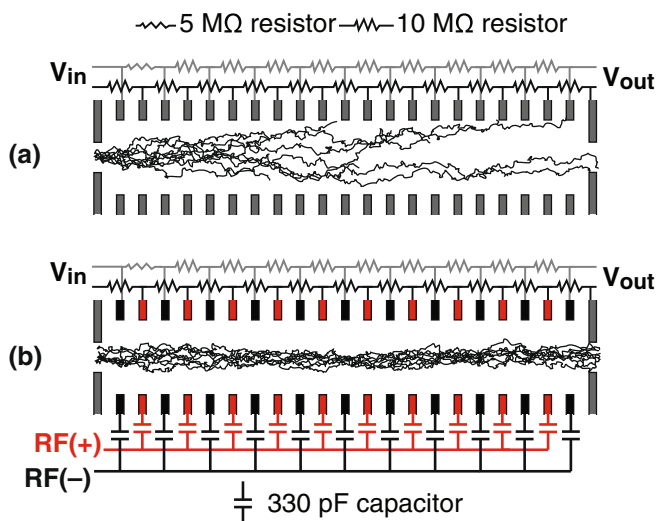


**Figure 1.** (a) Cross-sectional view of an electrostatic drift tube consisting of a series of ring electrodes connected to a voltage divider network that establishes a uniform DC gradient [ $(V_{in} - V_{out})/\text{drift length}$ ] across the axial drift region (x-direction). Ten ion trajectories of GRGDS $^{2+}$  are shown for a low  $E/P$  of  $0.507 \text{ V cm}^{-1} \text{Torr}^{-1}$ . (b) An rf-confining drift cell with the same physical dimensions and voltage divider network as (a), but that also applies a 2.8 MHz rf waveform to each electrode; the waveform applied to each electrode is  $180^\circ$  out of phase with that for the adjacent electrode. Under the same  $E/P$  as (a), an rf-confining drift cell exhibits increased ion transmission due to radial confinement. Note, this model is one-eighth of the actual drift cell length. All other ion simulations use a model that is one-third of the length of the actual drift cell

$\Omega$  determined with  $t_D$  acquired using rf confinement at both moderate and extremely low  $E/P$ .

### Effects of $V_{PP}$ on Drift Times, Transmission, and Resolving Power

The effects of varying rf peak-to-peak amplitude ( $V_{PP}$ ) from 15 to 200 V on the experimental arrival-time distributions of GRGDS $^{2+}$  under a moderate  $E/P$  ( $1.51 \text{ V cm}^{-1} \text{Torr}^{-1}$ ) was evaluated for a 7 mm (Fig. 2a) and 5 mm (Fig. 2b) i.d. rf-confining drift cell. Figure 2a shows that ion transmission in a 7 mm i.d. cell depends strongly on  $V_{PP}$ . In contrast, ion transmission in the 5 mm i.d. cell depends weakly on  $V_{PP}$  until  $V_{PP} < 25 \text{ V}$ . For a given i.d. cell, the centroids of arrival-time distribution are indistinguishable over the entire  $V_{PP}$  range. The resolving powers of the arrival-time distributions in both devices vary randomly within 2.8% of the average over the  $V_{PP}$  range investigated.

Figure 2c shows the experimental arrival-time distributions for GRGDS $^{2+}$  measured at  $V_{PP}$  ranging from 15 to 200 V in a 7 mm i.d. cell under a low  $E/P$  of  $0.507 \text{ V cm}^{-1} \text{Torr}^{-1}$ . Although the drift time increases 0.6% with increasing  $V_{PP}$ , this example demonstrates that ion drift times can be measured at extremely low  $E/P$ . In contrast to the 7 mm i.d. cell, the 5 mm

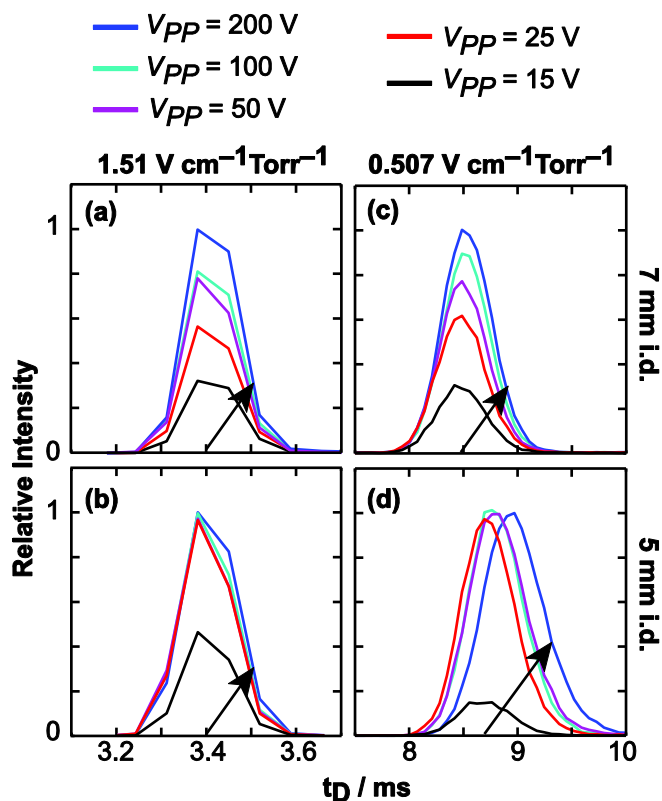


**Figure 2.** Experimental arrival-time distributions of GRGDS<sup>2+</sup> in 3.5 Torr helium in (a) and (c) 7 mm, and (b) and (d) 5 mm i.d. rf-confining drift cell under moderate and low  $E/P$  of (a) and (b) 1.51, and (c) and (d) 0.507 V cm<sup>-1</sup> Torr<sup>-1</sup>, respectively. Arrival-time distributions for each  $E/P$  and i.d. were acquired at five different rf peak-to-peak amplitudes ( $V_{PP}$ ) ranging from 15 to 200 V. The arrow represents increasing  $V_{PP}$  and the intensities are plotted relative to the  $V_{PP} = 200$  V peak in each panel. Absolute intensities are not included because data acquired using different i.d. drift cells were acquired on separate days using different electrospray emitters. At high  $V_{PP}$  voltages (>25 V) in the 5 mm i.d. rf-confining drift cell under extremely low  $E/P$  (d), arrival-time distributions shift to significantly longer drift times ( $t_D$ )

i.d. cell yields arrival-time distributions whose centroids increase up to 3% with  $V_{PP}$  from 15 to 200 V (Fig. 2d). Due to the rf component in the rf-confining drift cell,  $t_D$  can be measured at extremely low  $E/P$ . Note, the origin of the longer drift times observed in a 5 mm i.d. device (Fig. 2d) compared with 7 mm i.d. (Fig. 2c) is discussed in the next section.

Ion trajectory simulations were used to enable a direct comparison of the transmission, radial distribution, and resolving power of ions in an rf-confining drift cell relative to an electrostatic drift tube of the same dimensions. A discussion on the statistical approaches used in this analysis is described in the [Electronic Supplementary Material](#). At a drift field strength of 7.00 V cm<sup>-1</sup> Torr<sup>-1</sup> and after 8.4 cm in an electrostatic drift tube, 98% of the initial ions survive and have a beam waist of 3.6 mm, which is significantly greater than the diameter of the exit aperture of the drift cell (2.0 mm). Ions in an rf-confining

drift cell result in 100% transmission over that length and have a beam waist of 1.5 mm. The arrival-time distributions of the ions in the two devices at this field strength (Electronic Supplementary Material Figure S-1a) exhibit no significant difference in their average drift times, peak widths, or resolving powers (Electronic Supplementary Material Table S-1). At a drift field strength of 1.51 V cm<sup>-1</sup> Torr<sup>-1</sup> and after 8.4 cm in an electrostatic drift tube, 21% of the initial ions survive and have a beam waist of 4.0 mm. Ions in an rf-confining drift cell at 1.51 V cm<sup>-1</sup> Torr<sup>-1</sup> exhibit 100% transmission and a beam waste of 1.5 mm. Although the average drift time of ions in the rf-confining drift cell is slightly longer than those in the electrostatic drift tube (Electronic Supplementary Material Figure S-1b and Table S-1), there is no significant evidence that the resolving powers in the two devices are different.

### Effects of $E/P$ on Apparent Mobilities

To evaluate the effects of  $E/P$  on the apparent mobilities of ions, Fig. 3a shows experimental  $t_D$  of GRGDS<sup>2+</sup> measured using rf-confining drift cells with  $V_{PP} = 200$  V at 3.5 Torr helium. The data in Fig. 3a are plotted as a function of  $P/E$  (cm Torr V<sup>-1</sup>), which depends on drift length, pressure, and drift voltages used in these experiments. For a given set of data, pressures and drift cell length are constant; thus, changes in the x-axis depend only on the drift voltage. Figure 3b shows that  $t_D$  measured using the 7 mm i.d. cell agree well with the drift times calculated using Equation 2 ( $t_D^{ideal}$ ) for all  $E/P$  considered. In contrast, at extremely low  $E/P$  in the 5 mm i.d. cell, ions exhibit  $t_D$  that are up to 10% longer than expected at the lowest  $E/P$  (0.35 V cm<sup>-1</sup> Torr<sup>-1</sup>). Electronic Supplementary Material Figure S-2 shows that these  $t_D$  result in significant  $Q$  errors.

Ion trajectory simulations of GRGDS<sup>2+</sup> in rf-confining drift cells were then used to simulate drift times ( $t_D^{sim}$ ) over the same range of  $E/P$  used in the previous section (Electronic Supplementary Material Figure S-3). For each drift voltage, 150 ion trajectories were recorded, from which the averages and standard deviations were calculated. At low  $E/P$ ,  $t_D^{sim}$  of ions in a 5 mm i.d. cell are longer than  $t_D^{ideal}$  expected from Equation 2 and  $t_D^{sim}$  of ions in a 7 mm i.d. cell. These simulated results are consistent with the corresponding experimental data (Fig. 2).

### Origin of Mobility Dampening in rf-Confining Drift Cells

To investigate the origin of increased  $t_D$  at low  $E/P$ , the instantaneous, axial electric field ( $E_x^{sim}$ ) experienced by GRGDS<sup>2+</sup> was sampled at 20 MHz (i.e., faster than the 2.8 MHz frequency of the rf waveform). Next, the average  $E_x^{sim}$  was compared with the applied drift voltage divided by the drift cell length ( $E_x^{ideal}$ ). Figure 4a shows the simulated relative to the ideal electric field ( $\langle E_x^{sim} \rangle / E_x^{ideal}$ ) for GRGDS<sup>2+</sup> in rf-confining drift cells over a range of  $E/P$ . At moderate  $E/P$  (1.13 to 4.41 V cm<sup>-1</sup> Torr<sup>-1</sup>), the average electric field experienced by the ion in the two devices are indistinguishable. However, at extremely low  $E/P$ , ions in a 5 mm

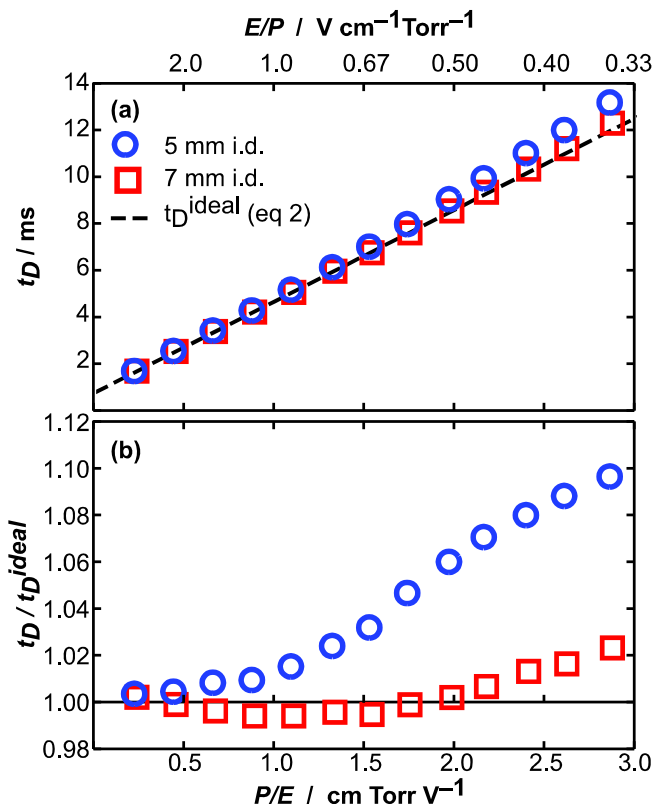


**Figure 3.** Experimental ion mobility data for GRGDS<sup>2+</sup> versus  $P/E$  acquired using a 5 mm (blue circles) or 7 mm (red squares) i.d. rf-confining drift cell with 3.5 Torr helium gas. (a) Drift times ( $t_D$ ) of GRGDS<sup>2+</sup> acquired using a 7 mm i.d. cell agree well with ideal drift times ( $t_D^{ideal}$ ) from Equation 2, whereas  $t_D$  in the 5 mm i.d. cell are longer than  $t_D^{ideal}$ . (b) Plotting  $t_D$  relative to  $t_D^{ideal}$  over a range of  $P/E$  show that  $t_D$  of GRGDS<sup>2+</sup> ions in a 5 mm i.d. cell are up to 10% longer than  $t_D^{ideal}$ . At extremely low  $E/P$ , insufficient field strengths at the beginning of the drift region may inhibit the injection of ions, which may contribute to the slight increase in 7 mm i.d. values in (b)

i.d. cell experience up to 5% less electric field compared with the ideal field, which is attributed to ions spending more time in lower field regions of the drift cell. This results in  $t_D^{sim.}$  that are longer than expected.

The effective potential ( $V_{eff}$ ), or pseudopotential, approximation is an alternative way to describe the electrical environment experienced by an ion that is moving slowly relative to the fast alternating rf potential [28]. Tolmachev et al. evaluated  $V_{eff}$  as [53]:

$$V_{eff}(r, z) = \frac{ze(V_{PP})^2}{16m\omega^2\delta^2 I_0^2(\rho/\delta)} \left[ I_1^2(r/\delta) \cos^2(z/\delta) + I_0^2(r/\delta) \sin^2(z/\delta) \right] \quad (4)$$

where  $z$  is the ion charge,  $e$  is the elementary charge,  $m$  is ion mass,  $\omega = 2\pi f$  where  $f$  is the rf frequency,  $\rho$  is the inner electrode radius,  $r$  is the radial position,  $z$  is the axial position,  $\delta = d/\pi$  where  $d$  is the center-to-center electrode spacing, and  $I_0$  and  $I_1$  are zero- and first-order modified Bessel functions, respectively. Radial focusing in ion funnels [30, 53, 54] and periodic-focusing DC-ion guides [41, 43] have been modelled previously using  $V_{eff}$ .

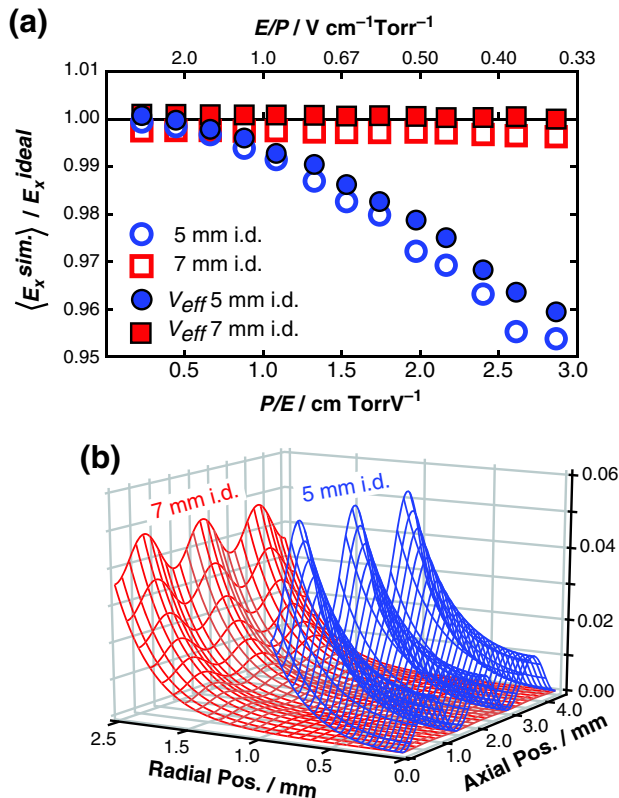


**Figure 4.** (a) The average of the instantaneous electric field ( $\langle E_x^{sim.} \rangle$ ) experienced by GRGDS<sup>2+</sup> during simulations of ion trajectories relative to ideal electric field ( $E_x^{ideal}$ , defined as the drift voltage divided by the drift cell length) plotted versus  $P/E$ . The open symbols show data for ions in a 5 mm (blue circles) or 7 mm (red squares) i.d. rf-confining drift cell. These values are compared with  $\langle E_x^{sim.} \rangle$  relative to  $E_x^{ideal}$  of GRGDS<sup>2+</sup> in an effective potential ( $V_{eff}$ ), which are plotted using closed symbols. Error bars are excluded because they are small compared with the marker size. (b) Zoomed regions (three electrodes) of  $V_{eff}$  (Equation 4) surfaces for GRGDS<sup>2+</sup> in a 5 mm (blue) or 7 mm (red) i.d. cell with no applied drift voltage,  $V_{PP} = 200$  V, and  $f = 2.8$  MHz. The full surfaces are shown in Electronic Supplementary Material Figure S-4

Electronic Supplementary Material Figure S-4 shows  $V_{eff}$  of GRGDS<sup>2+</sup> in rf-confining drift cells with  $f = 2.8$  MHz and  $V_{PP} = 200$  V with no drift voltage. This representation shows the pseudopotential environment that radially confines the trajectory of the ions; as ions diffuse in the radial directions, they experience elevated potentials that confine their trajectory. Closer examination of the  $V_{eff}$  surface reveals small pseudopotential wells in a 5 mm i.d. rf-confining drift cell that ions also experience (Fig. 4b). In other studies using ion funnels, reducing these pseudopotential wells by adjusting electrode dimensions was critical to reducing bias in  $m/z$  transmission [30, 53, 54].

To interpret the validity of  $V_{eff}$  to explain ion motion in an rf-confining drift cell, potential arrays of  $V_{eff}$  were constructed by superimposing a constant DC gradient onto Equation 4. These potential arrays were imported into SIMION and ion trajectories were simulated to calculate the average  $E_x^{sim.}$  compared

with  $E_x^{ideal}$  (Fig. 4a, solid data points). Interestingly, the average electric fields experienced by ions using  $V_{eff}$  are similar to those in trajectories that explicitly treated the rf potentials. Minor differences between the  $V_{eff}$  and rf-confining drift cell data sets (less than 1%) may be due to limitations in this effective potential approximation (Equation 4) or the use of a linear DC potential (rather than using a more accurate potential array for the electrostatic contributions).

These data show that in an rf-confining drift cell, pseudopotential wells generated by the rf potentials dampen the mobility of ions, and the magnitude of this effect depends on electrode dimensions and  $E/P$ . For example, experimental data in Fig. 2d show that ions in a 5 mm i.d. device have longer drift times than those in a 7 mm i.d. device (Fig. 2c) at low  $E/P$ . Additionally, this approach validates the use of  $V_{eff}$  to provide a robust, facile means of simulating ion trajectories with reduced computational cost. Electronic Supplementary Material Discussion and Figure S-5 provide a discussion and visual representation of the radial confinement and mobility dampening behavior of rf-confining drift cells as a function of electrode i.d. and  $V_{PP}$ . Briefly, similar radial confinement and mobility dampening effects can be achieved using both i.d. cells by adjusting  $V_{PP}$ . However, reducing mobility dampening by decreasing  $V_{PP}$  may also decrease ion transmission (Fig. 2). Another important consideration is the ion beam waist relative to the exit aperture of the drift cell (2 mm i.d.), which can reduce ion transmission for conditions at low  $V_{PP}$  or larger i.d. This is consistent with Fig. 2b and d, which show that for  $V_{PP} > 15$  V in a 5 mm i.d. cell, ion intensity stays constant due to ion beam waists being narrower than the exit aperture of the drift cell (in contrast to the 7 mm i.d. cell results in Fig. 2a and c). Operating at moderate  $V_{PP}$  (50 to 100 V) values enables mobility analysis with minimal transmission loss and negligible mobility dampening.

The mobility of an ion can also affect  $V_{eff}$ . For example, Tolmachev et al. introduced a pressure correction factor ( $\gamma$ ) to Equation 4 that depends on the mass of the ion,  $\Omega$ , pressure,  $f$ , and other factors [55]. Electronic Supplementary Material Discussion and Table S-2 show that for GRGDS<sup>2+</sup>,  $\gamma = 0.984$ ; a value of  $\gamma = 1$  represents no effect from the mobility on  $V_{eff}$ . To evaluate the contributions of mobility on  $V_{eff}$  for larger systems with lower mobility than GRGDS<sup>2+</sup>,  $\gamma$  for the 17+ charge state of the native-like, homotetramer of avidin (64 kDa) was calculated to be 0.999. This suggests that the mobilities of larger, native-like ions will not contribute significantly to the effectiveness of  $V_{eff}$ . Instead, the major contribution to  $V_{eff}$  of different ions is  $m/z$ ; according to Equation 4,  $V_{eff}$  is inversely proportional to  $m/z$ . According to this relationship, higher  $m/z$  ions will have both reduced mobility dampening and rf-confinement than lower  $m/z$  ions.

### Effective Temperatures

To gain insights into the effects of rf confinement on the effective temperature ( $T_{eff}$ ) of ions, ion trajectories of GRGDS<sup>2+</sup> in 3.5 Torr helium gas at 5.29 V cm<sup>-1</sup> (1.51 V

cm<sup>-1</sup> Torr<sup>-1</sup>) were simulated in rf-confining drift cells with  $V_{PP} = 200$  and 0 V (the latter is an electrostatic drift tube). All ion trajectories were simulated using a hard-sphere approximations model for ion-neutral collisions (described in Methods). Figure 5a (top panel) shows that ions in a 5 mm i.d. cell with  $V_{PP} = 0$  V experience a constant electric field ( $E_x$ ). In contrast, ions in a 5 mm i.d. cell with  $V_{PP} = 200$  V can briefly experience extremely high instantaneous  $E_x$  (up to 177 V cm<sup>-1</sup>) when between ring electrodes due to the alternating rf potentials (Fig. 5b, top panel). For comparison, GRGDS<sup>2+</sup> in an electrostatic drift tube with a constant  $E_x$  of 177 V cm<sup>-1</sup> would have a velocity of 3250 m s<sup>-1</sup>, which would yield a  $T_{eff}$  of ~1990 K, based on Equations 1 and 3, and result in rapid dissociation of peptide ions [56]. The instantaneous drift velocities ( $v_x$ ) of these ions are shown in Fig. 5 (middle panels). Although the distribution of  $v_x$  is broader in the presence of rf potentials (Fig. 5b), the peak  $v_x$  (585 m s<sup>-1</sup>, which would correspond to a  $T_{eff}$  of 353 K using Equation 3) is substantially less than that expected based on the peak  $E_x$ . Because the rf waveforms have such a high frequency (2.8 MHz), the ion does not accelerate substantially during a single rf cycle. For the ion trajectories shown in Fig. 5a and b, average  $E_x$  values (5.29 and 5.26 V cm<sup>-1</sup>, respectively) and  $v_x$  values (104.4 and 100.6 m s<sup>-1</sup>, respectively) are similar. Using these average  $v_x$  values and Equation 3, ions in an rf-confining drift cell with  $V_{PP} = 0$  or 200 V

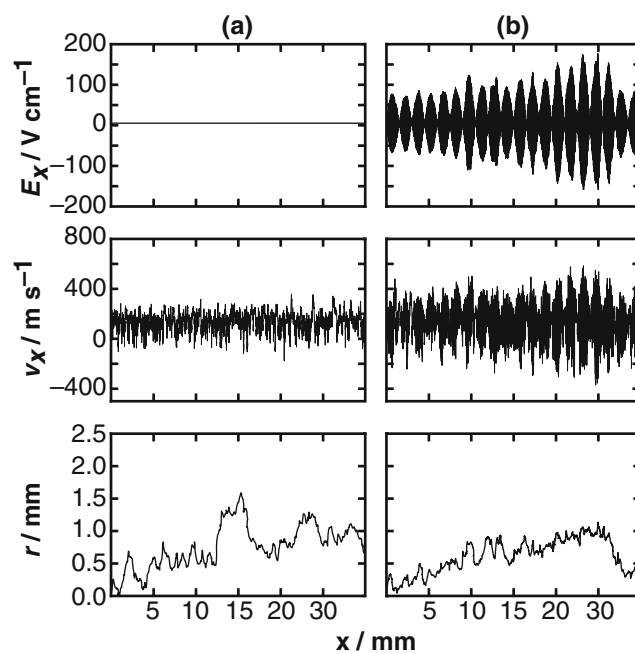


**Figure 5.** Ion trajectory simulations of GRGDS<sup>2+</sup> in 3.5 Torr helium buffer gas in a 5 mm i.d. rf-confining drift cell with  $V_{PP} =$  (a) 0 or (b) 200 V. All values are plotted versus the axial position along the drift cell ( $x$ ). The top panels show the instantaneous electric field experienced by the ion ( $E_x$ ), the middle panels show the instantaneous velocity ( $v_x$ ), and the bottom panels show the radial position of the ion ( $r$ ). Each plot consists of a single ion trajectory with  $E_x$ ,  $v_x$ , and  $r$  values sampled at 20 MHz. The  $x$ -axis only spans a small segment of the drift cell to better visualize subtle trends in data

have  $T_{eff}$  values of 299.9 or 299.8 K, respectively.

For a 5 mm i.d. cell,  $T_{eff}$  values determined using the peak and average  $v_x$  are different. A similar analysis performed for the 7 mm i.d. cell is shown in Electronic Supplementary Material Figure S-6, and the resulting  $T_{eff}$  values determined using the peak and average  $v_x$  are also very different. A summary of all  $T_{eff}$  values is shown in Electronic Supplementary Material Table S-3. It is challenging to determine whether the peak or average  $v_x$  is more appropriate, particularly since Equation 3 was derived for ions in an electrostatic drift tube [46]. Instead, an alternative approach was developed that depends on the distribution of relative ion-neutral speeds, rather than  $v_x$ .

In order to determine the distribution of relative ion-neutral speeds, populations of ion ( $v_i$ , where  $i = x, y,$  and  $z$ ) and neutral ( $V_i$ ) velocities were used;  $v_i$  values were sampled from ion trajectory simulations. All ion trajectories were simulated using the hard-sphere approximation collision model (described in Methods), during which  $v_i$  values were recorded just before an ion-neutral collision. For each  $E/P$ , greater than 800,000  $v_i$  values were recorded to generate a large ensemble for statistical comparisons. Populations of neutral gas velocities ( $V_i$ ) were sampled from a Maxwell-Boltzmann distribution at standard ambient temperature ( $T = 298.15$  K):

$$f(V_i) = \sqrt{\frac{M}{2\pi k_B T}} e^{-\frac{MV_i^2}{2k_B T}} \quad (5)$$

where  $M$  is the mass of the neutral (4.0 Da for helium). Relative ion-neutral speeds ( $s$ ) were then calculated:

$$s = \sqrt{\sum_{i=x,y,z} (v_i - V_i)^2} \quad (6)$$

Histograms of the ion-neutral speeds determined using this approach for GRGDS<sup>2+</sup> at 0 and 4.42 V cm<sup>-1</sup> Torr<sup>-1</sup> are shown in Electronic Supplementary Material Figure S-7a.

At equilibrium in the absence of an applied  $E$ , the relative ion-neutral speed distribution should be well-described by the Maxwell-Boltzmann distribution of relative speeds:

$$f(s) = \left(\frac{\mu}{2\pi k_B T}\right)^{3/2} 4\pi s^2 e^{-\frac{\mu s^2}{2k_B T}} \quad (7)$$

where  $\mu$  is the ion-neutral reduced mass. As expected, the Maxwell-Boltzmann speed distribution at 298.15 K and the histogram of speeds obtained in the absence of applied  $E$  are indistinguishable, but the histogram obtained for 4.42 V cm<sup>-1</sup> Torr<sup>-1</sup> is shifted towards higher speeds (Electronic Supplementary Material Figure S-7b). The difference between the histogram of speeds obtained for 4.42 V cm<sup>-1</sup> Torr<sup>-1</sup> and the Maxwell-Boltzmann speed distribution was minimized by optimizing  $T$  in Equation 7 using a Levenberg-Marquardt, least-squares minimization algorithm [57]. That process yielded a  $T$  of 311 K and the resulting Maxwell-Boltzmann speed

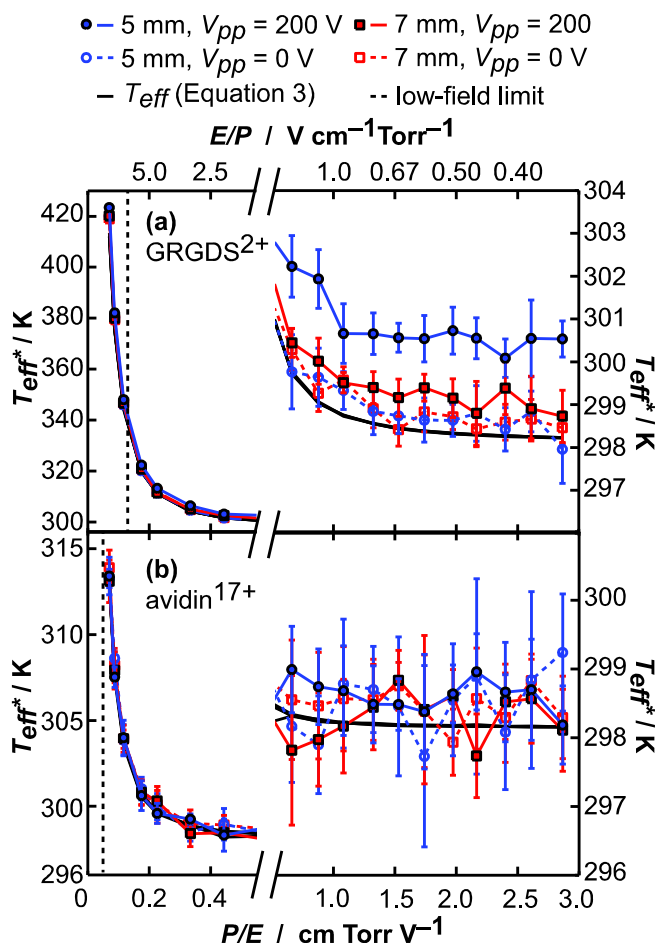
distribution is indistinguishable from the histogram of speeds (Electronic Supplementary Material Figure S-7c). Temperatures determined using this approach will be referred to as  $T_{eff}^*$  and represent the effective translational temperature of the ions in these simulations. Note that the structural dynamics of ions will depend on their internal-energy distributions, which will also depend on how efficiently energy is converted between translational and internal degrees of freedom. Therefore, the effective translational temperature likely represents the upper limit to the effective internal temperature of the ions.

Figure 6a shows  $T_{eff}^*$  values of GRGDS<sup>2+</sup> ions in 3.5 Torr helium buffer gas that were calculated from ion trajectory simulations of rf-confining drift cells with  $V_{PP} = 0$  V (analogous to an electrostatic drift tube) for a broad range of  $E$ .  $T_{eff}^*$  of GRGDS<sup>2+</sup> significantly increases at  $E/P$  values greater than 2 V cm<sup>-1</sup> Torr<sup>-1</sup> due to significantly higher  $v_i$  under these conditions. For  $E/P$  values lower than 2 V cm<sup>-1</sup> Torr<sup>-1</sup>,  $T_{eff}^*$  is relatively constant at ~299 K.  $T_{eff}^*$  values determined using the method above for ions when  $V_{PP} = 0$  V are indistinguishable from  $T_{eff}$  estimated from Equation 3 (Fig. 6a, black line), which validates using this approach to estimate effective temperatures.

Next, the above approach was used to estimate  $T_{eff}^*$  values for GRGDS<sup>2+</sup> ions in rf-confining drift cells with  $V_{PP} = 200$  V (Fig. 6a). These values show a similar increase to higher  $T_{eff}^*$  at  $E/P$  values higher than 2 V cm<sup>-1</sup> Torr<sup>-1</sup> compared with  $T_{eff}^*$  values from the  $V_{PP} = 0$  V devices. Interestingly, applied rf potentials in a 5 mm i.d. cell results, on average, in a 2 K increase in  $T_{eff}^*$  for a given  $E/P$  value compared with values determined using  $V_{PP} = 0$  V. In contrast to the  $T_{eff}$  results from Equation 3 (Fig. 6a, black line),  $T_{eff}^*$  results show that there is a systematic, yet subtle, increase in effective temperature for ions in a 5 mm i.d. rf-confining drift cell with  $V_{PP} = 200$  V.

Figure 6b shows  $T_{eff}^*$  values that were estimated for the 17+ charge state of the native-like, homotetramer of avidin. In contrast to GRGDS<sup>2+</sup> results,  $T_{eff}^*$  values for avidin<sup>17+</sup> are lower, particularly at the highest  $E/P$  conditions. Additionally, rf-confining drift cell i.d. and applied rf potential have no effect on the  $T_{eff}^*$  of these ions. For comparison,  $T_{eff}^*$  values were calculated using trajectories for GRGDS<sup>2+</sup> and avidin<sup>17+</sup> ions in 2 Torr helium gas to evaluate the effects of pressure (Electronic Supplementary Material Figure S-8).  $T_{eff}^*$  values calculated in 2 or 3.5 Torr helium differ, on average, by less than 0.03%, suggesting that lower pressures do not affect  $T_{eff}^*$  under these conditions.

In both i.d. rf-confining drift cells and at different helium buffer gas pressures, the application of rf potentials has minimal effect on the  $T_{eff}^*$  of ions. Instead,  $T_{eff}^*$  depends predominantly on  $E$  and the mobility of the analyte. For comparison, typical mobility conditions used in previous 7 mm i.d. rf-confining drift cell studies used  $E/P$  values of 2 to 7 V cm<sup>-1</sup> Torr<sup>-1</sup> [38, 39].  $T_{eff}^*$  of GRGDS<sup>2+</sup> at those limits are ~304 and 332 K, respectively (Fig. 6a). Thus, higher  $E$  in those experiments contribute to higher  $T_{eff}^*$  values, which may result in structural isomerization. For GRGDS<sup>2+</sup> at  $E/P$  of 7 V cm<sup>-1</sup> Torr<sup>-1</sup>, indistinguishable resolving powers were found for ion



**Figure 6.** Effective temperatures ( $T_{eff}^*$ ) of (a) GRGDS<sup>2+</sup> and (b) avidin<sup>17+</sup> in 3.5 Torr helium buffer gas as a function of  $P/E$ . The solid black line represents  $T_{eff}^*$  values calculated using the average  $v_x$  obtained from ion trajectory simulations and Equation 3.  $T_{eff}^*$  values calculated using least-squares minimization of relative-speed distributions to Maxwell-Boltzmann distributions are shown for ions in a 5 mm i.d.  $V_{PP} = 200$  V (solid blue circles), 5 mm i.d.  $V_{PP} = 0$  V (open blue circles), 7 mm i.d.  $V_{PP} = 200$  V (solid red squares), or 7 mm i.d.  $V_{PP} = 0$  V (open red squares) cell. (a)  $T_{eff}^*$  of GRGDS<sup>2+</sup> ions significantly increase (up to 420 K) at  $E/P$  values greater than  $2 \text{ V cm}^{-1} \text{ Torr}^{-1}$ . For comparison, the low-field limit [48] (dashed black line) of GRGDS<sup>2+</sup> ions is  $7.7 \text{ V cm}^{-1} \text{ Torr}^{-1}$ . Values lower than  $2 \text{ V cm}^{-1} \text{ Torr}^{-1}$  show that  $T_{eff}^*$  depends weakly on  $E/P$ .  $T_{eff}^*$  for ions measured in a 5 mm i.d. rf-confining drift cell with  $V_{PP} = 200$  V (solid blue circles) are systematically higher than those for the other conditions. (b)  $T_{eff}^*$  values at high  $E/P$  for avidin<sup>17+</sup> are significantly lower than those found in part a. For comparison, the low-field limit (dashed black line) of avidin<sup>17+</sup> ions is  $20 \text{ V cm}^{-1} \text{ Torr}^{-1}$ . All  $T_{eff}^*$  values of avidin<sup>17+</sup> are indistinguishable between different i.d. and  $V_{PP}$  and similar to values calculated using Equation 3. Error bars represent a 95% CI (Electronic Supplementary Material Figure S-7)

trajectory simulations using an electrostatic drift tube and an rf-confining drift cell (Electronic Supplementary Material Figure S-1a). This result suggests that the  $T_{eff}^*$  (332 K) and presence of rf-confining potentials do not affect the apparent

resolving power under these conditions, which is consistent with the experimental resolving powers of this ion being consistent with the diffusion of a single conformer over a wide range of  $E/P$  [38]. Because rf-confining drift cells enable measurements at extremely low  $E$ , adjusting drift voltage ranges to lower values enables mobility experiments with negligible contributions from field heating. Analogous analysis for the avidin 17+ data in Fig. 6b shows that  $T_{eff}^*$  values for  $E/P$  of 2 to  $7 \text{ V cm}^{-1} \text{ Torr}^{-1}$  range from 299 to 303 K, respectively. Because large native-like protein and protein complex ions have lower mobilities than peptide ions, they experience even less field-induced heating at a given  $E$ .

## Conclusions

The effects of rf confinement on the mobilities and effective temperatures of ions were evaluated using experimental results and computational models of rf-confining drift cells. For a wide range of  $E/P$  and  $V_{PP}$  values, the 7 mm i.d. rf-confining drift cell measures  $t_D$  that are similar to those expected for an analogous electrostatic drift tube (Fig. 3a). In contrast, for the lowest  $E/P$  used here, the 5 mm i.d. rf-confining drift cell exhibits  $t_D$  that are longer than expected. Using the effective potential approximation, ion trajectory simulations showed that mobility dampening occurs because of the presence of pseudopotential wells generated by alternating rf potentials (Fig. 4b), especially at high  $V_{PP}$  values. The effects of these pseudopotential wells on the mobility of ions is exacerbated at extremely low  $E/P$ . Mobility dampening in an rf-confining drift cell can be reduced by decreasing  $V_{PP}$ , but as a consequence, ion transmission may decrease. These results provide a fundamental framework for increasing the drift voltage parameter space and maintaining sufficient ion transmission in rf-confining drift cells, while not compromising the accuracy of resulting structural information.

The effective temperatures of ions were evaluated using ion trajectory simulations of the peptide GRGDS<sup>2+</sup> and protein complex avidin<sup>17+</sup> (Fig. 6). Analysis of the relative-speed distribution of the analyte and drift gas shows that the application of rf potentials has minimal effect on effective temperature. Rather, major contributions to effective temperatures are from drift-field induced heating at high  $E/P$ . These results assist in evaluating the effects of rf potentials on effective temperatures of ions over a broad range of  $E/P$  in rf-confining drift cells. The approach described in this work can be used to evaluate effective temperatures of ions in other IM devices containing rf potentials or other time-dependent electric fields.

This work demonstrates that rf-confining drift cells can operate under conditions (e.g., 7 mm i.d. and  $V_{PP}$  less than 200 V), in which Equations 1 and 2 are valid and  $\Omega$  determined using rf-confining drift cell measurements are indistinguishable from those determined using an electrostatic drift tube. Benefits of rf-confining drift cells, in which ions are confined radially throughout the entire separation, include that modest i.d. electrodes can be used for devices with long path lengths that can



be operated over a wide range of  $E/P$ . To maintain transmission for an electrostatic drift tube, the i.d. of electrodes must increase with increasing path length and decreasing  $E/P$  in order to ensure that ions are not lost prior to reaching a rear ion funnel. Advantages of reduced  $E/P$  measurements include reduced drift-field induced heating of the ions and longer drift times that reduce the contributions from other sources of peak broadening (e.g., ion gating). One disadvantage of rf-confining drift cells is that all electrodes are coupled to rf waveforms, which will become more challenging for significantly higher drift voltages due to dielectric breakdown of capacitors. Ultimately, this work shows that under the appropriate conditions, ion mobility devices may benefit from electrodynamic potentials, while retaining the fundamental ion separation principles used for traditional, electrostatic drift tubes.

## Acknowledgments

This material is based upon work supported by the National Science Foundation under CHE – 1550285 (M.F.B.), the University of Washington Research Royalty Fund under A70595 (M.F.B), and the American Chemical Society, Division of Analytical Chemistry Fellowship, sponsored by Agilent (S.J.A). M.F.B. thanks Professor Tyler H. McCormick (Department of Statistics and Department of Sociology, University of Washington) for suggesting the bootstrap for statistical analysis.

## References

- May, J.C., McLean, J.A.: Ion mobility-mass spectrometry: time-dispersive instrumentation. *Anal. Chem.* **87**, 1422–1436 (2015)
- Utrecht, C., Barbu, I.M., Shoemaker, G.K., van Duijn, E., Heck, A.J.R.: Interrogating viral capsid assembly with ion mobility-mass spectrometry. *Nat. Chem.* **3**, 126–132 (2011)
- Rabuck, J.N., Hyung, S.-J., Ko, K.S., Fox, C.C., Soellner, M.B., Ruotolo, B.T.: Activation state-selective kinase inhibitor assay based on ion mobility-mass spectrometry. *Anal. Chem.* **85**, 6995–7002 (2013)
- Zhou, M., Jones, C.M., Wysocki, V.H.: Dissecting the large noncovalent protein complex groel with surface-induced dissociation and ion mobility-mass spectrometry. *Anal. Chem.* **85**, 8262–8267 (2013)
- Zhou, M., Politis, A., Davies, R.B., Liko, I., Wu, K.-J., Stewart, A.G., Stock, D., Robinson, C.V.: Ion mobility-mass spectrometry of a rotary ATPase reveals ATP-induced reduction in conformational flexibility. *Nat. Chem.* **6**, 208–215 (2014)
- D'Agostino, P.A., Chenier, C.L.: Desorption electrospray ionization mass spectrometric analysis of organophosphorus chemical warfare agents using ion mobility and tandem mass spectrometry. *Rapid Commun. Mass Spectrom.* **24**, 1617–1624 (2010)
- Reynolds, J.C., Blackburn, G.J., Guallar-Hoyas, C., Moll, V.H., Bocos-Bintintan, V., Kaur-Atwal, G., Howdle, M.D., Harry, E.L., Brown, L.J., Creaser, C.S., Thomas, C.L.P.: Detection of volatile organic compounds in breath using thermal desorption electrospray ionization-ion mobility-mass spectrometry. *Anal. Chem.* **82**, 2139–2144 (2010)
- Campuzano, I., Bush, M.F., Robinson, C.V., Beaumont, C., Richardson, K., Kim, H., Kim, H.I.: Structural characterization of drug-like compounds by ion mobility mass spectrometry: comparison of theoretical and experimentally derived nitrogen collision cross sections. *Anal. Chem.* **84**, 1026–1033 (2012)
- Bush, M.F., Hall, Z., Giles, K., Hoyes, J., Robinson, C.V., Ruotolo, B.T.: Collision cross sections of proteins and their complexes: a calibration framework and database for gas-phase structural biology. *Anal. Chem.* **82**, 9557–9565 (2010)
- Lietz, C.B., Yu, Q., Li, L.: Large-scale collision cross-section profiling on a traveling wave ion mobility mass spectrometer. *J. Am. Soc. Mass Spectrom.* **25**, 2009–2019 (2014)
- Hofmann, J., Hahn, H.S., Seeberger, P.H., Pagel, K.: Identification of carbohydrate anomers using ion mobility-mass spectrometry. *Nature* **526**, 241–244 (2015)
- Groessl, M., Graf, S., Knochenmuss, R.: High resolution ion mobility-mass spectrometry for separation and identification of isomeric lipids. *Analyst* **140**, 6904–6911 (2015)
- Jurczek, E., Cruickshank, F., Porrini, M., Nikolova, P., Campuzano, I.D.G., Morris, M., Barran, P.E.: Intrinsic disorder in proteins: a challenge for (un)structural biology met by ion mobility-mass spectrometry. *Biochem. Soc. Trans.* **40**, 1021–1026 (2012)
- Ruotolo, B.T., Giles, K., Campuzano, I., Sandercock, A.M., Bateman, R.H., Robinson, C.V.: Evidence for macromolecular protein rings in the absence of bulk water. *Science* **310**, 1658–1661 (2005)
- Giles, K., Williams, J.P., Campuzano, I.: Enhancements in travelling wave ion mobility resolution. *Rapid Commun. Mass Spectrom.* **25**, 1559–1566 (2011)
- Silveira, J.A., Ridgeway, M.E., Park, M.A.: High resolution trapped ion mobility spectrometry of peptides. *Anal. Chem.* **86**, 5624–5627 (2014)
- Shelimov, K.B., Clemmer, D.E., Hudgins, R.R., Jarrold, M.F.: Protein structure in vacuo: gas-phase conformations of BPTI and cytochrome c. *J. Am. Chem. Soc.* **119**, 2240–2248 (1997)
- Kemper, P.R., Dupuis, N.F., Bowers, M.T.: A new, higher resolution, ion mobility mass spectrometer. *Int. J. Mass Spectrom.* **287**, 46–57 (2009)
- May, J.C., Goodwin, C.R., Lareau, N.M., Leaprot, K.L., Morris, C.B., Kurulugama, R.T., Mordehai, A., Klein, C., Barry, W., Darland, E., Overney, G., Imatani, K., Stafford, G.C., Fjeldsted, J.C., McLean, J.A.: Conformational ordering of biomolecules in the gas phase: nitrogen collision cross sections measured on a prototype high resolution drift tube ion mobility-mass spectrometer. *Anal. Chem.* **86**, 2107–2116 (2014)
- Dugourd, P., Hudgins, R.R., Clemmer, D.E., Jarrold, M.F.: High-resolution ion mobility measurements. *Rev. Sci. Instrum.* **68**, 1122–1129 (1997)
- Baker, E.S., Clowers, B.H., Li, F., Tang, K., Tolmachev, A.V., Prior, D.C., Belov, M.E., Smith, R.D.: Ion mobility spectrometry—mass spectrometry performance using electrodynamic ion funnels and elevated drift gas pressures. *J. Am. Soc. Mass Spectrom.* **18**, 1176–1187 (2007)
- Ibrahim, Y.M., Baker, E.S., Danielson III, W.F., Norheim, R.V., Prior, D.C., Anderson, G.A., Belov, M.E., Smith, R.D.: Development of a new ion mobility time-of-flight mass spectrometer. *Int. J. Mass Spectrom.* **377**, 655–662 (2015)
- Mason, E.A., McDaniel, E.W.: Transport properties of ions in gases, p. 276. Wiley, New York (1988)
- Revercomb, H.E., Mason, E.A.: Theory of plasma chromatography/gaseous electrophoresis - a review. *Anal. Chem.* **47**, 970–983 (1975)
- Tang, K., Shvartsburg, A.A., Lee, H.-N., Prior, D.C., Buschbach, M.A., Li, F., Tolmachev, A.V., Anderson, G.A., Smith, R.D.: High-sensitivity ion mobility spectrometry/mass spectrometry using electrodynamic ion funnel interfaces. *Anal. Chem.* **77**, 3330–3339 (2005)
- Guevremont, R., Siu, K.W.M., Wang, J., Ding, L.: Combined ion mobility/time-of-flight mass spectrometry study of electrospray-generated ions. *Anal. Chem.* **69**, 3959–3965 (1997)
- Gillig, K.J., Ruotolo, B., Stone, E.G., Russell, D.H., Fuhrer, K., Gonin, M., Schultz, A.J.: Coupling high-pressure MALDI with ion mobility/orthogonal time-of-flight mass spectrometry. *Anal. Chem.* **72**, 3965–3971 (2000)
- Gerlich, D.: In state selected and state-to state ion-molecule reaction dynamics. part 1. experiment. Wiley, New York (1992)
- Kim, T., Tolmachev, A.V., Harkewicz, R., Prior, D.C., Anderson, G., Udseth, H.R., Smith, R.D., Bailey, T.H., Rakov, S., Futrell, J.H.: Design and implementation of a new electrodynamic ion funnel. *Anal. Chem.* **72**, 2247–2255 (2000)
- Lynn, E.C., Chung, M.C., Han, C.C.: Characterizing the transmission properties of an ion funnel. *Rapid Commun. Mass Spectrom.* **14**, 2129–2134 (2000)
- Javahery, G., Thomson, B.: A segmented radiofrequency-only quadrupole collision cell for measurements of ion collision cross section on a triple quadrupole mass spectrometer. *J. Am. Soc. Mass Spectrom.* **8**, 697–702 (1997)
- McCullough, B.J., Kalapothakis, J., Eastwood, H., Kemper, P., MacMillan, D., Taylor, K., Dorin, J., Barran, P.E.: Development of an Ion mobility quadrupole time of flight mass spectrometer. *Anal. Chem.* **80**, 6336–6344 (2008)

33. Covey, T., Douglas, D.J.: Collision cross-sections for protein ions. *J. Am. Soc. Mass Spectrom.* **4**, 616–623 (1993)
34. Gill, A.C., Jennings, K.R., Wyttenbach, T., Bowers, M.T.: Conformations of biopolymers in the gas phase: a new mass spectrometric method. *Int. J. Mass Spectrom.* **195/196**, 685–697 (2000)
35. Thalassinos, K., Slade, S.E., Jennings, K.R., Scrivens, J.H., Giles, K., Wildgoose, J., Hoyes, J., Bateman, R.H., Bowers, M.T.: Ion mobility mass spectrometry of proteins in a modified commercial mass spectrometer. *Int. J. Mass Spectrom.* **236**, 55–63 (2004)
36. Zucker, S.M., Ewing, M.A., Clemmer, D.E.: Gridless overtone mobility spectrometry. *Anal. Chem.* **85**, 10174–10179 (2013)
37. Tolmachev, A.V., Webb, I.K., Ibrahim, Y.M., Garimella, S.V.B., Zhang, X., Anderson, G.A., Smith, R.D.: Characterization of ion dynamics in structures for lossless ion manipulations. *Anal. Chem.* **86**, 9162–9168 (2014)
38. Allen, S.J., Giles, K., Gilbert, T., Bush, M.F.: Ion mobility mass spectrometry of peptide, protein, and protein complex ions using a radio frequency-confining drift cell. *Analyst* **141**, 884–891 (2016)
39. Allen, S.J., Schwartz, A.M., Bush, M.F.: Effects of polarity on the structures and charge states of native-like proteins and protein complexes in the gas phase. *Anal. Chem.* **85**, 12055–12061 (2013)
40. Silveira, J.A., Jeon, J., Gamage, C.M., Pai, P.-J., Fort, K.L., Russell, D.H.: Damping factor links periodic focusing and uniform field ion mobility for accurate determination of collision cross sections. *Anal. Chem.* **84**, 2818–2824 (2012)
41. Silveira, J.A., Gamage, C.M., Blase, R.C., Russell, D.H.: Gas-phase ion dynamics in a periodic-focusing DC ion guide. *Int. J. Mass Spectrom.* **296**, 36–42 (2010)
42. Blase, R.C., Silveira, J.A., Gillig, K.J., Gamage, C.M., Russell, D.H.: Increased ion transmission in IMS: a high resolution, periodic-focusing DC ion guide ion mobility spectrometer. *Int. J. Mass Spectrom.* **301**, 166–173 (2011)
43. Gamage, C.M., Silveira, J.A., Blase, R.C., Russell, D.H.: Gas-phase ion dynamics in a periodic-focusing DC ion guide (Part II): Discrete transport modes. *Int. J. Mass Spectrom.* **303**, 154–163 (2011)
44. Freeke, J., Bush, M.F., Robinson, C.V., Ruotolo, B.T.: Gas-phase protein assemblies: unfolding landscapes and preserving native-like structures using noncovalent adducts. *Chem. Phys. Lett.* **524**, 1–9 (2012)
45. Hall, Z., Politis, A., Bush, M.F., Smith, L.J., Robinson, C.V.: Charge-state dependent compaction and dissociation of protein complexes: insights from ion mobility and molecular dynamics. *J. Am. Chem. Soc.* **134**, 3429–3438 (2012)
46. Mason, E.A., McDaniel, E.W.: In: *Transport properties of ions in gases*, p. 149. Wiley, New York (1988)
47. Mason, E.A., McDaniel, E.W.: *Transport properties of ions in gases*, p. 154. Wiley, New York (1988)
48. Mason, E.A., McDaniel, E.W.: *Transport properties of ions in gases*, p. 4. Wiley, New York (1988)
49. Shvartsburg, A.A., Smith, R.D.: Fundamentals of traveling wave ion mobility spectrometry. *Anal. Chem.* **80**, 9689–9699 (2008)
50. Morsa, D., Gabelica, V., De Pauw, E.: Effective temperature of ions in traveling wave ion mobility spectrometry. *Anal. Chem.* **83**, 5775–5782 (2011)
51. Merenbloom, S.I., Flick, T.G., Williams, E.R.: How hot are your ions in TWAVE ion mobility spectrometry? *J. Am. Soc. Mass Spectrom.* **23**, 553–562 (2011)
52. Dahl, D.: SIMION. version 8.0; Idaho National Engineering Laboratory: Idaho Falls, ID
53. Tolmachev, A.V., Kim, T., Udseth, H.R., Smith, R.D., Bailey, T.H., Futrell, J.H.: Simulation-based optimization of the electrodynamic ion funnel for high sensitivity electrospray ionization mass spectrometry. *Int. J. Mass Spectrom.* **203**, 31–47 (2000)
54. Shaffer, S.A., Tolmachev, A., Prior, D.C., Anderson, G.A., Udseth, H.R., Smith, R.D.: Characterization of an improved electrodynamic ion funnel interface for electrospray ionization mass spectrometry. *Anal. Chem.* **71**, 2957–2964 (1999)
55. Tolmachev, A.V., Chemushevich, I.V., Dodonov, A.F., Standing, K.G.: A collisional focusing ion guide for coupling an atmospheric pressure ion source to a mass spectrometer. *Nucl. Instrum. Methods Phys. Res. B* **124**, 112–119 (1997)
56. Schnier, P.D., Price, W.D., Jockusch, R.A., Williams, E.R.: Blackbody infrared radiative dissociation of bradykinin and its analogues: energetics, dynamics, and evidence for salt-bridge structures in the gas phase. *J. Am. Chem. Soc.* **118**, 7178–7189 (1996)
57. Marquardt, D.W.: An algorithm for least-squares estimation of nonlinear parameters. *J. Appl. Math.* **11**, 431–441 (1963)